JACS
JOURNAL OF THE AMERICAN CHEMICAL SOCIETY

Article

pubs.acs.org/JACS

Thermal Stabilization of Metal–Organic Framework-Derived Single-Site Catalytic Clusters through Nanocasting

Camille D. Malonzo,[†] Sammy M. Shaker,[†] Limin Ren,[‡] Steven D. Prinslow,[†,§] Ana E. Platero-Prats,[∥] Leighanne C. Gallington,[∥] Joshua Borycz,[†] Anthony B. Thompson,[†] Timothy C. Wang,[⊥] Omar K. Farha,[⊥,#] Joseph T. Hupp,[⊥] Connie C. Lu,[†] Karena W. Chapman,[∥] Jason C. Myers,[¶] R. Lee Penn,[†] Laura Gagliardi,[†] Michael Tsapatsis,[‡] and Andreas Stein*[,†]

[†]Department of Chemistry, University of Minnesota, 207 Pleasant Street SE, Minneapolis, Minnesota 55455, United States

[‡]Department of Chemical Engineering and Materials Science, University of Minnesota, 421 Washington Avenue SE, Minneapolis, Minnesota 55455, United States

[§]Department of Chemistry, Austin College, 900 North Grand Avenue, Sherman, Texas 75090, United States

[∥]X-ray Science Division, Advanced Photon Source, Argonne National Laboratory, 9700 South Cass Avenue, Argonne, Illinois 60439, United States

[⊥]Department of Chemistry and Chemical and Biological Engineering, Northwestern University, 2145 Sheridan Road, Evanston, Illinois 60208, United States

[#]Department of Chemistry, Faculty of Science, King Abdulaziz University, Jeddah, Saudi Arabia

[¶]College of Science and Engineering Characterization Facility, University of Minnesota, 100 Union Street SE, Minneapolis, Minnesota 55455, United States

Supporting Information

ABSTRACT: Metal–organic frameworks (MOFs) provide convenient systems for organizing high concentrations of single catalytic sites derived from metallic or oxo-metallic nodes. However, high-temperature processes cause agglomeration of these nodes, so that the single-site character and catalytic activity are lost. In this work, we present a simple nanocasting approach to provide a thermally stable secondary scaffold for MOF-based catalytic single sites, preventing their aggregation even after exposure to air at 600 °C. We describe the nanocasting of NU-1000, a MOF with 3 nm channels and Lewis-acidic oxozirconium clusters, with silica. By condensing tetramethylorthosilicate within the NU-1000 pores via a vapor-phase HCl treatment, a silica layer is created on the inner walls of NU-1000. This silica layer provides anchoring sites for the oxozirconium clusters in NU-1000 after the organic linkers are removed at high temperatures. Differential pair distribution functions obtained from synchrotron X-ray scattering confirmed that isolated oxozirconium clusters are maintained in the heated nanocast materials. Pyridine adsorption experiments and a glucose isomerization reaction demonstrate that the clusters remain accessible to reagents and maintain their acidic character and catalytic activity even after the nanocast materials have been heated to 500–600 °C in air. Density functional theory calculations show a correlation between the Lewis acidity of the oxozirconium clusters and their catalytic activity. The ability to produce MOF-derived materials that retain their catalytic properties after exposure to high temperatures makes nanocasting a useful technique for obtaining single-site catalysts suitable for high-temperature reactions.

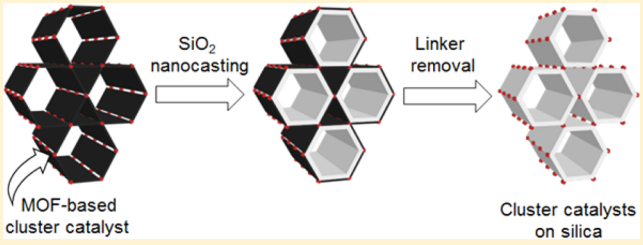

INTRODUCTION

In the pursuit of highly active heterogeneous catalysts, great emphasis has been placed on the catalyst surface, as mainly the surface atoms are involved in the catalytic reactions. The importance of this active surface has prompted efforts to convert bulk systems to nanoparticles and porous materials, where the reduced size and porosity work to increase the accessible surface area in these materials and thereby enhance reaction rates. Even with these systems, however, the ratio of surface to nonsurface atoms is still small. Structural defects and nonuniformity of the catalyst surface also exist, which can lead to poor selectivity in the reaction products. The need for a catalyst system that combines high catalytic activity and selectivity has thus sparked an interest in single catalytic sites—single atoms or small, well-defined clusters of atoms stabilized as discrete units on a support.[1] Single metal sites arguably maximize catalytic activity per metal compared to their nanoparticle counterparts.[2] Product selectivity can also be expected because these identical, structurally well-defined sites

Received: December 4, 2015
Published: February 5, 2016

DOI: 10.1021/jacs.5b12688
J. Am. Chem. Soc. 2016, 138, 2739–2748

should have similar electronic and spatial interactions with reactant molecules.[3−6]

A key to promoting the catalytic activity of these single sites is to distribute them at high loadings in a heterogeneous system, which requires porous, high surface area supports. Microporous zeolites have been used as supports for these single sites and have become some of the most important catalyst systems in the industry.[7] Recently, significant focus has been directed to metal−organic frameworks (MOFs),[8−11] which in comparison with zeolites are a more diverse class of materials in terms of both structure and composition. MOFs are porous materials that consist of metal ions or clusters interconnected via organic linkers. The metal or cluster sites in the MOF themselves can be catalytic,[12−17] and these materials can be modified postsynthetically to install other single-site metals.[18−22] Thus, it is possible to tune the reactivity of a MOF-based catalyst by engineering the catalytic metal sites, first with the choice of metal present in the framework itself and then by postsynthetic modification.[23] In addition, larger pore sizes have been achieved in MOFs than in zeolites, providing easy reactant access to the catalytic sites present in the MOF structure.[24,25]

One drawback of MOFs, however, is their limited thermal stability. Most MOFs can only withstand temperatures of about 150−350 °C in air.[20,26−29] Above these temperatures, the organic linkers that connect the catalytic metal sites in the MOF structure decompose, leading to the aggregation of the metal sites and loss of their catalytic activity. For this reason, MOFs cannot be used to catalyze reactions that occur only at high temperatures, including a number of industrially important reactions, such as alkane dehydrogenation and water gas shift reactions.[30,31] Faster reaction rates are also attained if catalysts can operate at high temperatures, which makes catalysts with high thermal stability desirable. To take advantage of the highly tunable catalytic metal sites in MOFs for high-temperature catalysis, it is therefore necessary to stabilize the sites so that they remain isolated from each other and accessible even after the linkers are lost at these high temperatures.

Inspired by nanocasting techniques developed extensively for mesoporous materials,[32] we have developed an approach to stabilize the MOF cluster sites by supporting them in a secondary porous skeleton that is maintained at high temperatures. A few examples of nanocasting in MOFs exist in the literature, where the target structure is an inverse replica of the original MOF and all of the original material is removed.[33−38] In the product structures described here, only the organic linkers are eliminated, while the catalytic oxometal cluster sites are kept embedded in a thermally stable matrix where they remain isolated from each other and accessible to reactants. In this work, we report the preparation of a silica nanocast of NU-1000,[18] a MOF composed of hexanuclear oxozirconium clusters ($[Zr_6(\mu_3\text{-}O)_4(\mu_3\text{-}OH)_4(OH)_4(H_2O)_4]^{8+}$) and 1,3,6,8-tetrakis(*p*-benzoate)pyrene linkers ($TBAPy^{4-}$) (Figure 1a). When NU-1000 is heated to a temperature at which the oxozirconium clusters lose coordinated water (Figure 1b), it becomes a Lewis acid catalyst, showing superior activity, for example, in the catalytic breakdown of known chemical warfare agents.[16] We determined the Lewis acid activity of the oxozirconium clusters experimentally by measuring the catalytic activity and using theory by computing the reaction mechanism of glucose isomerization and analyzing the atomic charges in the clusters throughout the reaction. We demonstrate that the nanocast NU-1000 maintains this activity after the organic linkers have been removed from the structure by high-temperature treatment. We also show that through nanocasting with silica aggregation of the oxozirconium clusters of NU-1000 is prevented after the linkers are removed. Thus, a high concentration of these well-dispersed catalytic sites is maintained in a thermally stable material that is now suitable for catalytic processes that may require high temperatures.

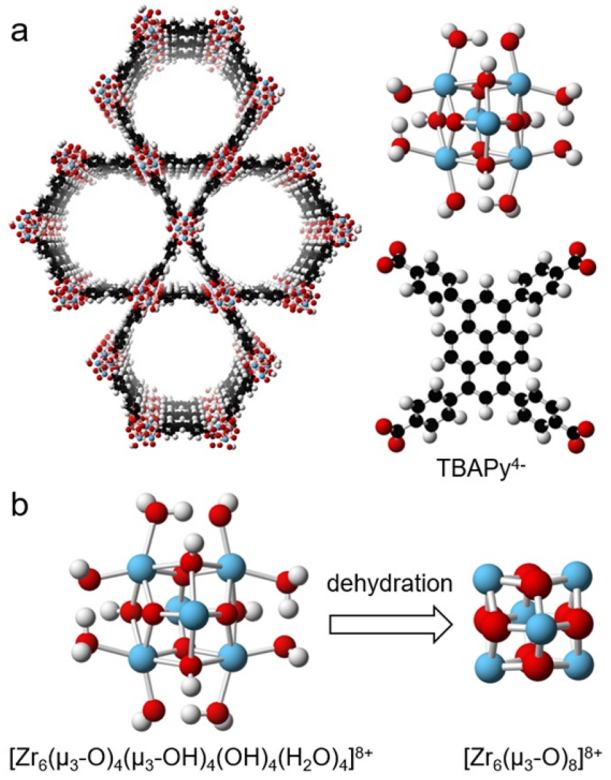

Figure 1. (a) Structure of NU-1000 showing the oxozirconium clusters ($[Zr_6(\mu_3\text{-}O)_4(\mu_3\text{-}OH)_4(OH)_4(H_2O)_4]^{8+}$) and organic linkers ($TBAPy^{4-}$) that make up the framework. (b) Dehydration of the oxozirconium clusters converts them to the Lewis acidic form ($[Zr_6(\mu_3\text{-}O)_8]^{8+}$). Color code: Zr (blue); O (red); C (black); H (white).

EXPERIMENTAL METHODS

Materials. The following chemicals were used as received: tetramethyl orthosilicate (TMOS, 98%), methanol (≥99.8%), $ZrOCl_2{\cdot}8H_2O$ (98%), benzoic acid (99.5%), pyridine (99.8%), and D-glucose (≥99.5%) from Sigma-Aldrich; acetone (98%) and *N*,*N*-dimethylformamide (DMF, 99.8%) from Macron Fine Chemicals; and hydrochloric acid (36.5−38.0%) from BDH Chemicals. The linker, 1,3,6,8-tetrakis(*p*-benzoic acid)pyrene (H_4TBAPy) was synthesized as previously described.[20] Deionized water produced on-site with a minimum resistivity of 18.2 MΩ·cm was used in all experiments.

Nanocasting NU-1000 with Silica. NU-1000 was synthesized following a previously reported method (details in the Supporting Information).[39] To prepare a silica nanocast of NU-1000, 300 μL of TMOS and 5 μL of H_2O were first sonicated in a vial for 10 min. The mixture was then added to 30 mg of activated NU-1000 and allowed to infiltrate the MOF particles for 24 h. The infiltrated sample was washed with methanol twice to remove the TMOS on the external surface of the NU-1000 particles and then heated at 50 °C for 5 min to dry. To induce polycondensation of TMOS within the sample, the sample was first exposed to HCl vapor for 24 h at room temperature. This was followed by heat treatment in a closed vial at 60 °C for another 24 h. The resulting nanocast material is referred to as SiO_2@NU-1000. This material was heated to 500 °C using a

DOI: 10.1021/jacs.5b12688
J. Am. Chem. Soc. 2016, 138, 2739−2748

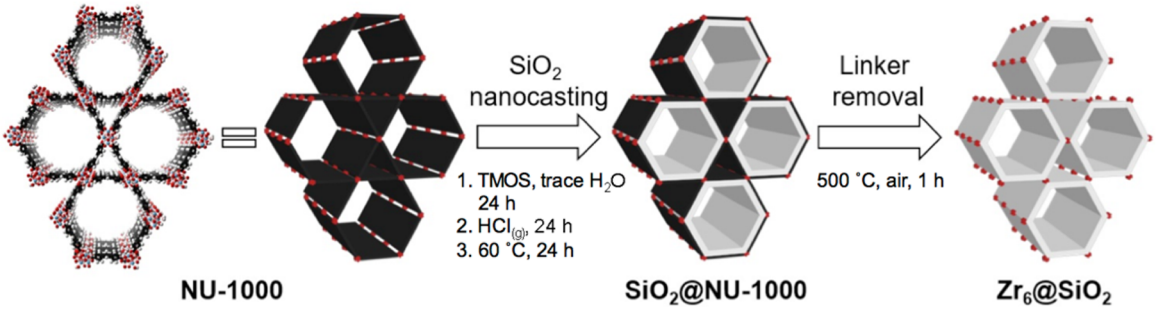

Figure 2. Scheme for the process of stabilizing the oxozirconium clusters in NU-1000 by nanocasting with silica. The image on the left represents the NU-1000 structure with cluster nodes (red) and linkers (black). The white layer in the middle image represents silica.

temperature ramp rate of 2 °C/min and maintained at that temperature in air for 1 h to remove the organic linkers from the structure. The resulting product is denoted as Zr_6@SiO_2. To determine the limits of thermal stabilization, SiO_2@NU-1000 was also independently calcined at 600 and 700 °C for 1 h using a ramp rate of 2 °C/min. The resulting samples are denoted as Zr_6@SiO_2 (600 °C) and Zr_6@SiO_2 (700 °C), respectively.

Pyridine Adsorption. The Lewis and Brønsted acid sites on Zr_6@SiO_2 were detected using pyridine as a probe molecule. The sample was placed under dynamic vacuum (<200 mTorr) at 200 °C for 1 h to remove surface-adsorbed water. After cooling to room temperature, the sample was placed under static vacuum, and excess pyridine was injected through a septum. The reaction with pyridine was allowed to proceed for 1 h. The sample was placed under dynamic vacuum again at 200 °C for 1 h to remove any physisorbed pyridine and then cooled to room temperature. Pyridine adsorption was then analyzed by FT-IR spectroscopy.

Catalyst Testing: Glucose Isomerization. The catalytic performance of Zr_6@SiO_2 was tested using the Lewis-acid-catalyzed isomerization reaction of glucose to fructose as a model reaction. This reaction, carried out at a low temperature (90 °C), allows assessment of the retention of catalytic performance against the original NU-1000 structure which is stable at this temperature. In a typical reaction, 0.03 g of D-glucose, 2.97 g of ethanol, and 0.012 g of the catalyst were added into a 20 mL thick-walled glass reactor and sealed with a crimp top (PTFE/silicone septum) from VWR. The reactor was placed in an oil bath at 90 °C at specific reaction times, and the reaction was quenched afterward by placing the reactor in an ice bath. The catalyst was then filtered out, and deionized H_2O (3.87 g) was added to the reaction solution to hydrolyze ethylated sugars at 90 °C for 2 days. All reactants and products were analyzed by HPLC. Aside from NU-1000, the catalytic performance of the nanocast material was tested against other samples including calcined NU-1000 and control samples of oxozirconium clusters in nontemplated silica (see Supporting Information for the detailed synthesis of the control samples).

Computational Methods. Density functional theory (DFT) has proven to be helpful for determining the structure[39] and reactivity[19] of NU-1000. To aid in our understanding of the effectiveness of the oxozirconium clusters in NU-1000 and in Zr_6@SiO_2 as Lewis acid catalytic sites, we computed the reaction mechanism of glucose isomerization at these clusters. The free energies (ΔG) of each mechanistic step were computed using the dehydrated oxozirconium cluster model described by Planas et al.[39] with the eight linkers truncated to formic acid groups (Figure S1). Each step of the reaction pathway was fully optimized with the M06-L[40] density functional in Gaussian 09[41,42] in the gas phase. The optimizations were performed with the 6-31G(d) basis set on C, H, and O and the Stuttgart/Dresden effective core potential (SDD)[43] on Zr. Frequency calculations at 298 K were also performed at this level to find the transition states. Single-point frequency calculations at the same temperature were then performed on these equilibrium and transition state structures with the def2-TZVP basis set[44] to extract free energies. The relative free energies were computed by subtracting the free energy of glucose bound to the oxozirconium cluster model from the free energy of each reaction step. Mulliken charges were computed for the Zr and O atoms in the cluster as indicators of the change of Lewis acidity along the glucose isomerization reaction path.

Instrumentation. FT-IR spectra were collected on a Nicolet Magna-IR 760 spectrometer. Thermogravimetric analysis (TGA) was carried out using a Netzsch STA 409 PC Luxx instrument. Scanning electron microscopy (SEM) measurements were performed on a JEOL 6700 scanning electron microscope operated using a 3.0 kV accelerating voltage. Prior to SEM analysis, all samples were sputter coated with a conductive thin film (50 Å) of Pt. X-ray diffraction (XRD) patterns were collected using an X'Pert Pro diffractometer with an X'Celerator detector. A Co anode (Kα, λ = 1.789 Å) operated at 45 kV and 40 μA was used as the radiation source. Simulated XRD patterns of tetragonal ZrO_2 (PDF #50-1089) were generated using Mercury[45] based on Scherrer line widths for different crystallite sizes. Inductively coupled plasma–optical emission spectrometry (ICP-OES) using a Thermo Scientific iCAP 6500 analyzer was employed for the determination of the Zr content in the samples. High-performance liquid chromatography (HPLC) with a Bio-Rad Aminex HPX87C (300 × 7.8 mm) column and refractive index detector was used for all reactant and product analyses during the catalytic tests. The mobile phase was ultrapure water (pH = 7), and the column temperature was 80 °C. The C, H, and N content in Zr_6@SiO_2 (500 °C) was determined to be 0.2, 1.1, and 0.0 wt %, respectively, using combustion analysis by Atlantic Microlab, Norcross, GA.

N_2 sorption analyses were conducted using a Quantachrome Autosorb iQ2. The NU-1000 and SiO_2@NU-1000 samples were degassed at 120 °C, and the Zr_6@SiO_2 and control samples were degassed at 200 °C, at 1 mTorr for 12 h prior to the analysis. Brunauer–Emmett–Teller (BET) surface areas were evaluated from the adsorption isotherms within the 0.08–0.28 P/P_o range. Pore size distributions and surface area histograms were obtained using DFT (Quantachrome, N_2 at 77 K on carbon or silica, slit pore) methods.

Transmission electron microscopy (TEM) images were collected on an FEI Tecnai G^2 field-emission S/TEM operating at an accelerating voltage of 300 kV. High-angle annular dark field (HAADF) images were collected on an E. A. Fischione annular detector at a camera length of 120 mm, which yields an inner collection semiangle of 49.8 mrad. Energy-dispersive X-ray spectroscopy (EDS) spectra were collected using an EDAX RTEM thin-window detector. To provide sufficient X-ray intensity for the maps and line-scans, the sample was tilted to the detector takeoff angle of 15°. EDS line scans and maps were collected using a pixel dwell time of 16 s, a beam convergence semiangle of 9.2 mrad, and a probe current of ~0.5 nA. Data were analyzed using FEI TIA software (version 4.5) and Gatan Digital-Micrograph software (version 1.84).

Synchrotron X-ray Structure Analysis. X-ray scattering data suitable for pair distribution function (PDF) and diffraction analysis were collected at beamline 11-ID-B at the Advanced Photon Source at Argonne National Laboratory. High-energy X-rays (wavelength 0.2114 Å, 58.6 keV) were used in combination with a large amorphous silicon-based area detector. For PDF analysis, total scattering data were collected using a short sample-to-detector distance (~18 cm) to Q_{max} = 23 $Å^{-1}$. For diffraction analysis, data with improved angular

DOI: 10.1021/jacs.5b12688
J. Am. Chem. Soc. 2016, 138, 2739–2748

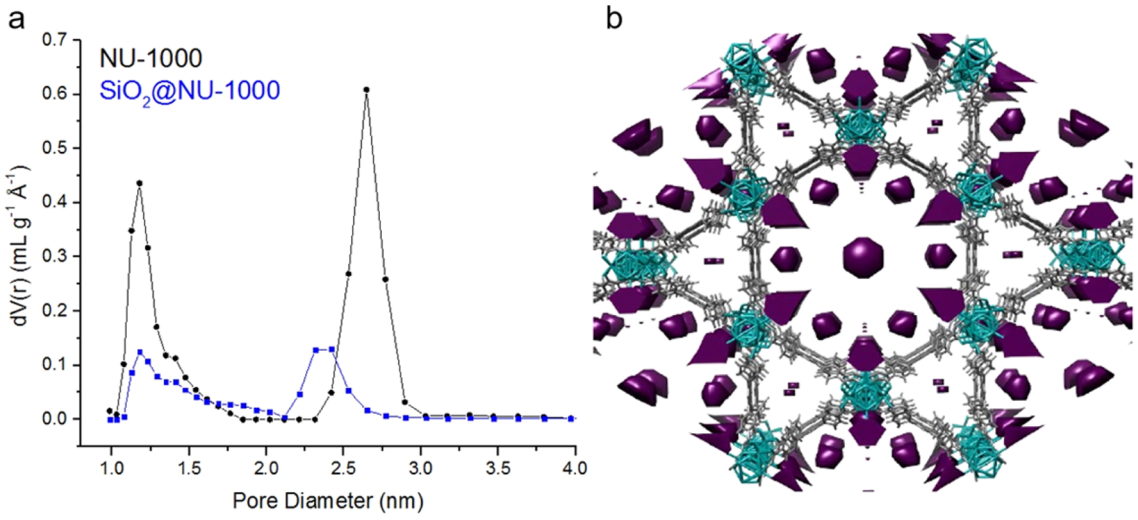

Figure 3. (a) DFT pore size distribution of NU-1000 (BET surface area = 2064 m^2 g^{-1}, pore volume = 1.44 cm^3 g^{-1}) before and after nanocasting with SiO_2 (BET surface area = 901 m^2 g^{-1}, pore volume = 0.55 cm^3 g^{-1}). (b) Difference envelope density analysis data showing the new electron density (SiO_2, purple) after nanocasting NU-1000 (oxozirconium clusters in teal, organic linkers in gray).

resolution were collected at longer sample-to-detector distance (~95 cm). The X-ray scattering images were reduced within QXRD and FIT2D.[46,47]

A difference envelope density (DED) analysis[48,49] was applied to diffraction data to evaluate the distribution of SiO_2 within the crystalline NU-1000 framework. The diffuse contributions to the background were removed by subtracting scattering measured for an empty sample capillary and amorphous SiO_2.[50−52] The Bragg peak intensities for pristine and nanocast NU-1000 were determined by performing Le Bail whole pattern fits to the diffraction data within the *P6/mmm* space group of the parent phase,[20] refining the hexagonal lattice parameters and pseudo-Voigt profile parameters. Structure envelopes were generated based on the low-index reflections, as described previously.[48,53] A difference envelope, reflecting the distribution of silica within the NU-1000 lattice, was generated by taking the difference between the envelopes for SiO_2@NU-1000 and an unmodified NU-1000 sample.

Pair distribution functions (PDFs) were extracted from the total scattering data within PDFgetX2, correcting for background and Compton scattering.[54] Data were collected for pristine NU-1000, SiO_2@NU1000, Zr_6@SiO_2, TMOS-derived silica, and the control Zr_6@n-t-SiO_2. Differential analyses were applied to separate the contributions from silica from the oxozirconium clusters or NU-1000 lattice. Structure models were refined against the differential PDFs (dPDFs) within PDFgui to evaluate the particle size of the Zr-based clusters following thermal treatment.

RESULTS AND DISCUSSION

Silica Nanocasting. Silica nanocasts of NU-1000 were prepared according to the scheme shown in Figure 2. The silica precursor, tetramethylorthosilicate (TMOS), is small enough to fit in the 3 nm pores of NU-1000, allowing the precursor to infiltrate these pores. Under hydrolytic conditions, TMOS can then be condensed in the presence of an acid catalyst to form silica within the NU-1000 framework. Our earlier attempts to nanocast NU-1000 with silica used a mixture of TMOS, aqueous HCl, and methanol as the casting fluid (see Supporting Information for details). The added methanol was necessary to slow down the silica formation during infiltration, which could otherwise lead to pore blockage, hindering percolation through the entire NU-1000 particle. However, that method yielded mainly extra-framework silica, with virtually no shift to lower pore size for the 3 nm channels in NU-1000, indicating that

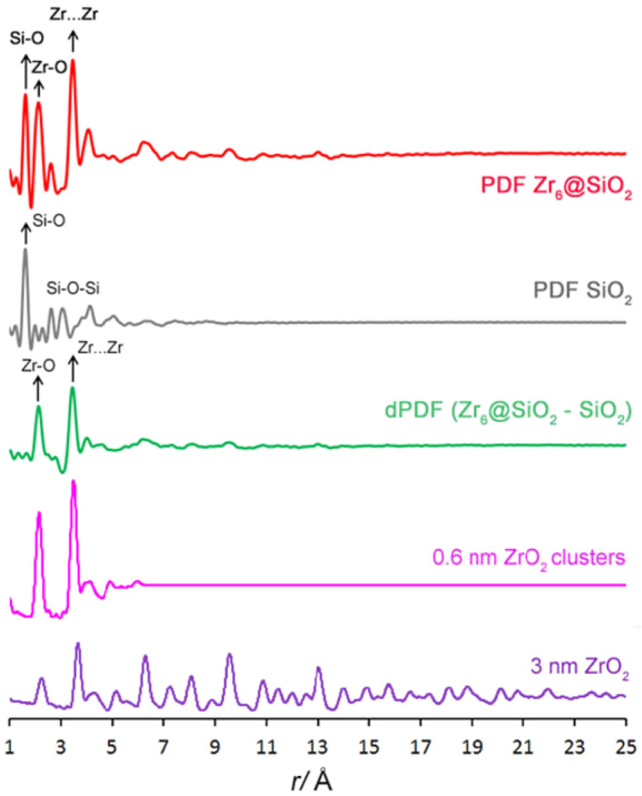

Figure 4. PDFs for Zr_6@SiO_2 and an amorphous silica sample, dPDF, for Zr_6@SiO_2 showing new Zr−O and Zr···Zr correlations and PDFs for the oxozirconium clusters (0.6 nm, $Fm\bar{3}m$, a = 4.88 Å) and larger cubic ZrO_2 particles (3 nm, $Fm\bar{3}m$, a = 4.88 Å).

only a small amount of silica was present in these pores (Figure S2). This could be due to TMOS occupying only 68% of the precursor solution volume. Because both H_2O and HCl as an acid catalyst are present in the precursor solution, TMOS hydrolysis and oligomerization is also possible, yielding short silica chains that could already be too large to infiltrate into the NU-1000 pores. Multiple infiltration steps were carried out

DOI: 10.1021/jacs.5b12688
J. Am. Chem. Soc. 2016, 138, 2739−2748

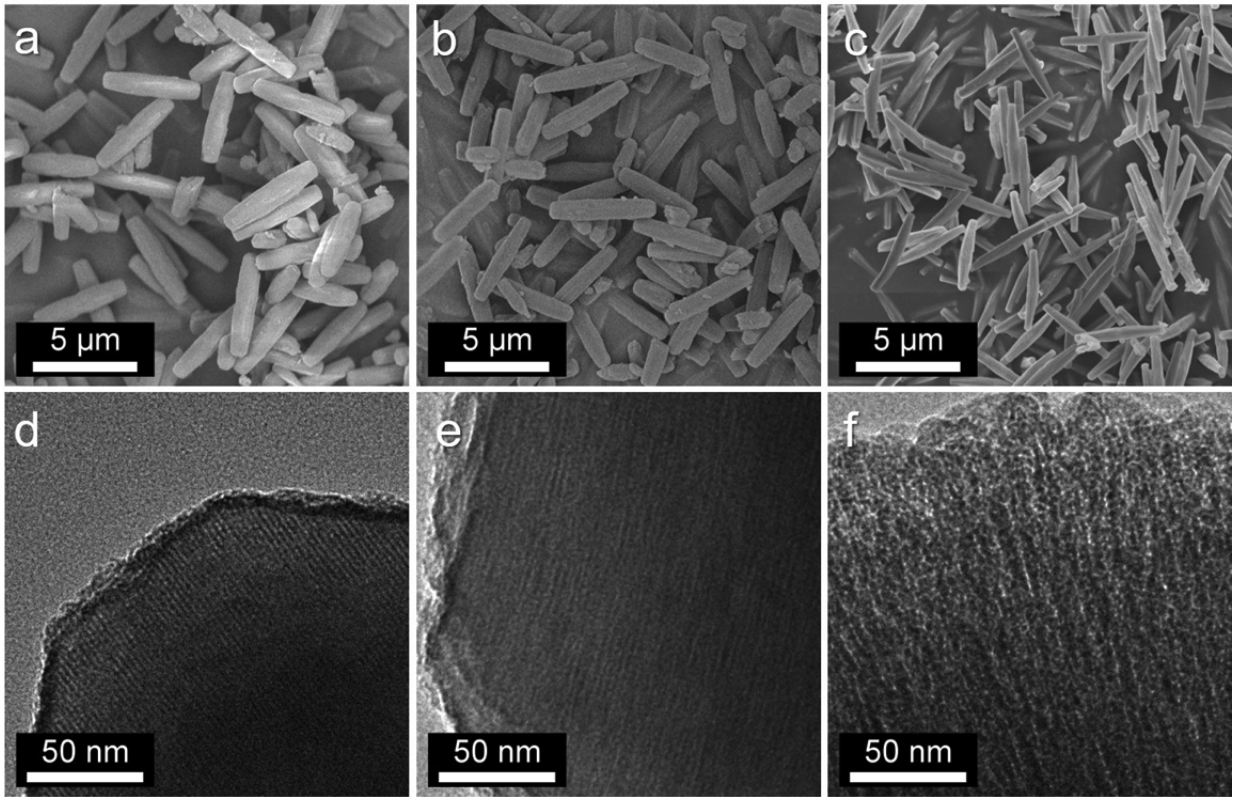

Figure 5. SEM (a–c) and TEM (d–f) images of NU-1000 (a, d), SiO_2@NU-1000 (b, e), and Zr_6@SiO_2 (c, f).

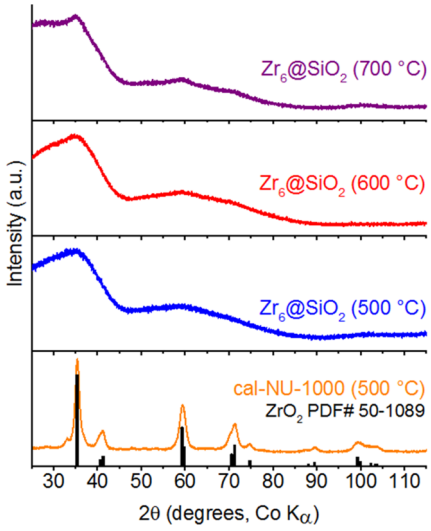

Figure 6. XRD patterns of Zr_6@SiO_2 after heat treatment at 500, 600, or 700 °C in air. For comparison, the XRD pattern of NU-1000 calcined at 500 °C in air is also shown. The line pattern corresponds to the published powder diffraction file pattern for tetragonal ZrO_2 (powder diffraction file #50–1089).

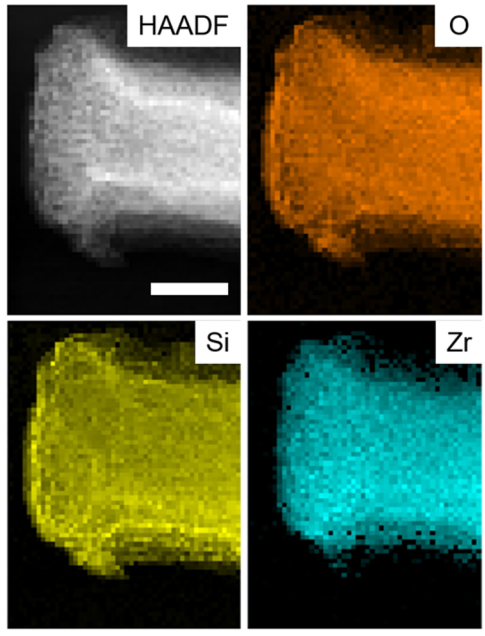

Figure 7. High-angle annular dark field (HAADF) image and STEM-EDS elemental maps of Zr_6@SiO_2. The scale bar corresponds to 200 nm.

using this method, but this did not improve the silica loading in the pores (Figure S2).

Instead, to raise the amount of silica in the pores of NU-1000, we increased the fraction of TMOS in the casting fluid to 98% v/v, the balance being water. As TMOS hydrolysis and condensation occur instantaneously when HCl is added to this mixture, the acid must be introduced (via vapor-phase HCl treatment) only after the mixture has percolated through the NU-1000 pores. The presence of silica in the product obtained after nanocasting was confirmed by the appearance of an intense absorption at 1090 cm^{-1} in the FT-IR spectrum (Figure S3) related to the Si–O–Si stretching vibration. While the total amount of silica in this nanocast product is approximately the same as in the sample from the original nanocasting method (TGA data, Figure S4), a larger proportion of it is present within the NU-1000 framework as shown by the greater shift in

DOI: 10.1021/jacs.5b12688
J. Am. Chem. Soc. 2016, 138, 2739–2748

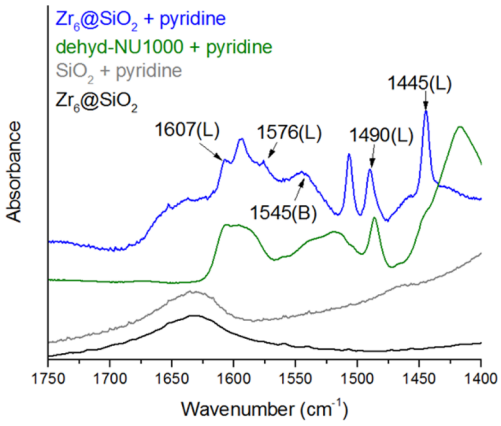

Figure 8. FT-IR spectra showing pyridine adsorption data for Zr_6@SiO_2 (500 °C) and dehyd-NU-1000. The peaks indicate the presence of accessible Lewis (L) and Brønsted (B) acid sites in the samples. The spectra of Zr_6@SiO_2 (500 °C) (before pyridine adsorption) and SiO_2 (after pyridine adsorption) are also shown for comparison.

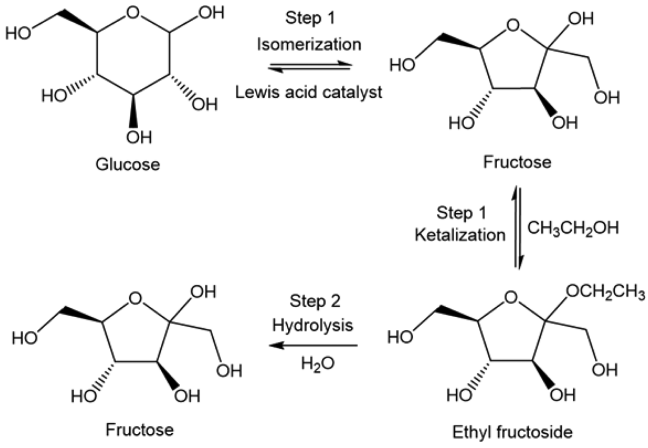

Figure 9. Reaction scheme for the isomerization of glucose to fructose. Adapted from Saravanamurugan et al.[59] The computed reaction mechanism is provided in Figure S11.

the DFT pore size distribution of the sample (Figure 3a). The pore radius decreased by ca. 0.2 nm upon infiltration of the larger hexagonal channels in NU-1000, while the smaller trigonal channels maintained their original dimensions.

The diffraction and pair distribution function (PDF) data demonstrate that the NU-1000 framework structure is maintained through the nanocasting procedure. The presence of Bragg diffraction peaks indicates that the long-range crystalline ordering of the lattice is preserved (Figure S5). The differential PDF trace, subtracting the contributions from the new silica phase, shows the same local structures in the pristine and nanocast systems (Figure S6), characterized by a feature at ∼1.4 Å associated with the C−C and C−O bonds in the $TBAPy^{4-}$ linker, and features at ∼2.1 and 3.5 Å associated with the Zr−O and Zr···Zr′ atom−atom distances, respectively.

The difference envelope density (DED) analysis, based on the low-index Bragg reflections, provides a map of electron density added to the NU-1000 pores following the silica nanocasting (Figure 3b). This analysis shows that the silica is primarily deposited in a layer on the surface of the 3 nm hexagonal channels close to the oxozirconium nodes and organic linkers, with almost no silica in the smaller 1 nm trigonal pores. This is also reflected in the decrease in intensity of the 010 reflection following nanocasting (Figure S5)—this peak corresponds to the 3 nm channel spacing in NU-1000. The reduced electron contrast following silica incorporation into these channels leads to reduced intensity of this 010 peak. As suggested by the nitrogen sorption data (Figure 3a), there is no shift in the pore size for the trigonal pores indicating no significant silica electron density within these small pores. The distribution of the silica as a layer on the pore surface of the hexagonal channels provides a secondary skeleton or framework structure that can serve as a scaffold for the oxozirconium clusters following removal of the organic linkers at high temperature.

Cluster Stabilization at High Temperatures. An ultimate aim is to use these nanocast products to catalyze reactions at high temperatures. To be useful for high-temperature catalysis, however, the silica backbone in the nanocast materials should be able to serve as a support for the Lewis acidic oxozirconium clusters in place of the organic linkers that are lost at these temperatures. Site isolation and accessibility of these clusters are necessary to maintain high Lewis acid catalytic activity. To determine whether this high-temperature cluster stabilization was achieved through nanocasting, we removed the organic linkers in the nanocast material (SiO_2@NU-1000) by calcination, which leaves only the oxozirconium clusters and the silica matrix (Zr_6@SiO_2).

The dPDF trace for Zr_6@SiO_2 (Figure 4, 0−8 Å region highlighted in Figure S7) shows that the organic linkers were eliminated, with no peaks at ∼1.4 Å from C−C or C−O bonds within the linkers. This is consistent with chemical analysis that detected only 0.2 wt % of carbon in the sample. The dPDF is dominated by peaks at ∼2.14 and ∼3.47 Å associated with Zr−O and Zr···Zr correlations within oxozirconium clusters, respectively. Structural models, based on cubic ZrO_2, were refined against the dPDF data, using a spherical particle parameter to estimate the ZrO_2 particle size distribution. The nanocast Zr_6@SiO_2 was dominated by small ∼0.6 nm clusters ZrO_2 (∼95%, a = 4.88 Å) with a minor component of larger ∼3

Table 1. Properties of Catalysts Tested for Glucose Isomerization

sample	Zr content[a] (% w/w)	maximum synthesis temperature (°C)	BET surface area[b] (m^2 g^{-1})	pore volume (cm^3 g^{-1})[b]
Zr_6@SiO_2	23	500	444	0.46
dehyd-NU-1000	30	300	2100	1.61
cal-NU-1000	74	500	52	0.13
Zr_6@n-t-SiO_2	0.7	500	371	0.32
Zr_6@n-t-SiO_2(High Zr)	9	500	173	0.12

[a]The Zr content of dehyd-NU-1000 and cal-NU-1000 was estimated assuming the formulas $Zr_6(\mu_3\text{-}O)_8(HTBAPy)_2$ and ZrO_2, respectively. The Zr content of nanocast Zr_6@SiO_2 and the control samples, Zr_6@n-t-SiO_2 and Zr_6@n-t-SiO_2(High Zr), were determined by ICP-MS. [b]The N_2 sorption isotherms and DFT surface area versus pore size histograms are shown in Figure S10.

DOI: 10.1021/jacs.5b12688
J. Am. Chem. Soc. 2016, 138, 2739−2748

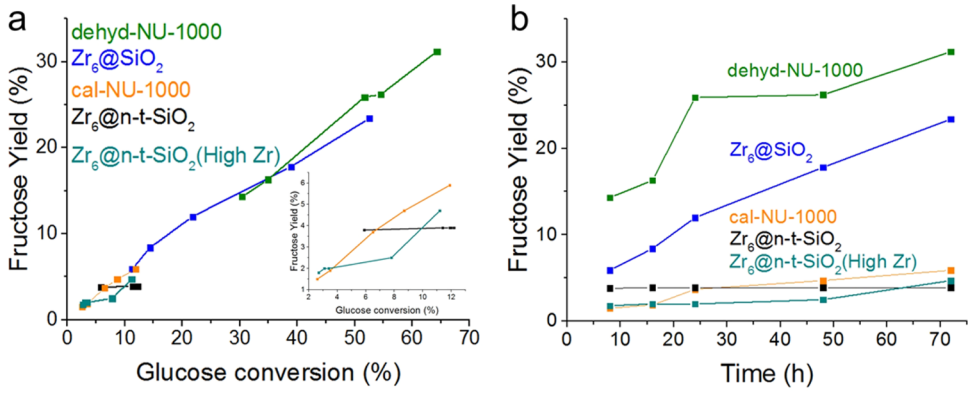

Figure 10. (a) Fructose yield versus glucose conversion and (b) fructose yield versus time over different catalysts.

nm nanoparticles, modeled as cubic ZrO_2 with significant O disorder (~5%, a = 5.11 Å). The retention of such a large fraction of the small ~0.6 nm clusters suggests that the nanocasting approach is successful in improving the thermal stability of the clusters. While aggregation was not entirely eliminated in the nanocast system, it may be expected that oxozirconium clusters closer to the outer surface of the particles may be more susceptible to aggregation, and the larger nanoparticles observed in this case may be associated with clusters near the surface. Alternatively, small domains of NU-1000 not penetrated by the silica precursor could account for the minor phase of aggregated ZrO_2 nanoparticles.

Figure 5 shows electron micrographs tracking the progression from NU-1000 to the nanocast material SiO_2@NU-1000 and to the final product after removal of the linkers, Zr_6@SiO_2. There is no significant change in morphology after nanocasting (Figure 5b), and the lattice fringes from the 3 nm channels are still observable from the high magnification TEM image of the nanocast products (Figure 5e). This is consistent with the XRD data which shows a low angle peak at 2θ = 3° that corresponds to structural features on the ~3 nm scale (Figure S5). After the linkers are removed by heating the sample at 500 °C in air, the particles shrink, and the TEM image shows a more disordered structure (Figure 5c, 5f). This is accompanied by a decrease in BET surface area (from 944 to 444 m^2 g^{-1}) and pore volume (from 0.55 to 0.46 cm^3 g^{-1}) due to the loss of micropores in the structure. Of particular interest is the XRD pattern of this sample, which does not exhibit any notable diffraction peaks (Figure 6, Zr_6@SiO_2 (500 °C)). On the other hand, a noninfiltrated NU-1000 sample that was heated to the same temperature (cal-NU-1000) exhibits diffraction peaks that can be indexed to the tetragonal phase of ZrO_2 (Figure 6, cal-NU-1000 (500 °C)). This difference is also reflected in the selected area electron diffraction (SAED) patterns of the two samples (Figure S8), where cal-NU-1000 shows diffraction rings that index to tetragonal ZrO_2, which are absent in the SAED pattern of Zr_6@SiO_2. The presence of the diffraction patterns in the XRD and SAED data indicates that in cal-NU-1000 the oxozirconium clusters have aggregated at the high treatment temperatures to form larger ZrO_2 crystallites (ca. 18 nm calculated from the XRD line broadening using the Scherrer equation), which would cause a loss in catalytic activity because agglomeration reduces the number of exposed Lewis acid sites. The absence of notable diffraction peaks in Zr_6@SiO_2 demonstrates that, by nanocasting with SiO_2, we are able to prevent the oxozirconium clusters from aggregating after the linkers are removed at high temperatures, in agreement with the dPDF data.

The SiO_2@NU-1000 samples were also calcined at 600 and 700 °C to determine the limits of thermal stabilization. As shown in Figure 6, the broad features are still maintained at 600 °C, indicating that there is still no significant cluster aggregation at this temperature. At 700 °C, some peaks are visible in the pattern, but these are still not as prominent as in the case of cal-NU-1000. We simulated the Scherrer broadening of the XRD peaks of tetragonal ZrO_2 for different crystallite sizes (Figure S9). From this we estimate that for Zr_6@SiO_2 heated to 600 °C the crystallites are still single, isolated clusters (ca. ~ 0.6 nm). The clusters start to aggregate at 700 °C, but the aggregate size is still significantly smaller (<2 nm) compared to the case of cal-NU-1000 (ca. 18 nm) that was heated to only 500 °C.

STEM-EDS elemental maps (Figure 7) of the nanocast products after linker removal show a homogeneous distribution of O, Si, and Zr throughout the material. For Si in particular, there is no Si-deficient core, which indicates that uniform infiltration was achieved during nanocasting. This presumably afforded the site isolation of the clusters, as the presence of silica throughout the particle can provide proximal anchor sites for these clusters. Additionally, the EDS map also shows only a very thin outer layer of silica on the sample surface, not a thick crust which would prevent access to the catalytic clusters within the particles.

Lewis Acidity and Catalytic Performance of Nanocast NU-1000. NU-1000 is an excellent Lewis acid catalyst owing to the high concentration of the Lewis acidic oxozirconium clusters in its structure, which are easily accessible through its mesoporous channels.[16] In particular, the Lewis acidity can be enhanced by dehydration of the clusters, which eliminates terminal aquo and hydroxo ligands and converts hydroxo bridges to oxo bridges, thereby reducing the number of oxide-based species that bind to the Zr(IV) centers.[16] Similar cluster dehydration processes are expected during the heat treatment at 500 °C to form Zr_6@SiO_2 and open up Zr(IV) sites. To determine whether the Lewis acidic clusters in the nanocast materials remain accessible, we carried out a pyridine adsorption experiment on Zr_6@SiO_2. Pyridine is a common IR probe for detecting acidic sites in solid acid catalysts. The peaks for the ring vibrations of pyridine, which appear in the region between 1700 and 1400 cm^{-1}, shift depending on whether pyridine is coordinated to a Lewis acid site or is protonated by a Brønsted acid site.[55] After pyridine adsorption, the FT-IR spectrum of Zr_6@SiO_2 shows peaks for pyridine adsorbed on Lewis acid sites (Figure 8). These peaks

DOI: 10.1021/jacs.5b12688
J. Am. Chem. Soc. 2016, 138, 2739−2748

correspond to the normal modes ν_{8a} and ν_{19a} of the ring-breathing (νCCN) vibrations of pyridine with A_1 symmetry (1607 and 1490 cm^{-1}, respectively) and the ν_{8b} and ν_{19b} modes with B_2 symmetry (1576 and 1445 cm^{-1}, respectively),[56] all in close agreement with those found for Lewis-site coordinated pyridine on ZrO_2.[57] Similar peaks are observed for pyridine adsorbed on dehydrated NU-1000. It is interesting to note that the pyridine peaks are less well resolved in the case of dehydrated NU-1000, possibly due to additional interactions of the probe molecule with linkers between oxozirconium clusters. Evidence for some Brønsted acidity is also present in both the Zr_6@SiO_2 sample and the dehydrated NU-1000, as indicated by a vibrational band at 1545 cm^{-1} typical for pyridinium ions bonded to Brønsted sites.[57] Amorphous silica prepared from TMOS using the same treatment as for Zr_6@SiO_2 shows no corresponding absorption bands in the FT-IR spectrum. The pyridine adsorption data confirm that the clusters are accessible in the nanocast material, which is facilitated through its high surface area and mesoporous structure (Figure S10). We estimated the ratios of Lewis-to-Brønsted acid sites (L:B) in the Zr_6@SiO_2 (500 °C) and dehyd-NU-1000 samples by integrating the peaks at 1445 and 1545 cm^{-1} in Figure 8 (see Table S1 for the peak integration values). Absorption coefficients from Rosenberg and Anderson[58] were used to estimate relative acid site concentrations from the peak areas. While the resulting L:B ratios of 0.46 for Zr_6@SiO_2 and 0.24 for dehyd-NU-1000 have some uncertainty due to peak fitting procedures, they show that the relative L:B content did not decrease after nanocasting and probably increased slightly, most likely because removal of the organic linkers exposed more Lewis acid sites on the clusters. More importantly, these data show that both materials contain appreciable amounts of Brønsted and Lewis acid sites, and both sites remain accessible to pyridine molecules.

The catalytic activity of the oxozirconium clusters was tested with the Lewis-acid-catalyzed isomerization of glucose to fructose. As this reaction occurs at low temperatures, the catalytic performance of the clusters in the nanocast Zr_6@SiO_2 and the original NU-1000 structure can be compared. We used DFT calculations to determine the mechanism of glucose isomerization on the clusters (Figure S11). The dehydrated, Lewis acidic form of the clusters, $[Zr_6(\mu_3\text{-}O)_8]^{8+}$, features two Zr and two μ_3-O sites on each face of the cluster structure (Figure 1b), which work in tandem to stabilize protonic and oxidic moieties that form during the isomerization reaction. The Mulliken partial charges of the Zr atoms in the bare oxozirconium cluster are ~1.75. Throughout the reaction, the charges of the two Zr atoms on the reacting face fluctuate between 1.50 and 1.69 (Table S2), indicating that both Zr atoms are acting as electron acceptors to stabilize the intermediate species throughout the glucose isomerization. A more detailed description of the mechanism is provided together with the reaction scheme in the Supporting Information. The largest transition state barrier in the mechanism is 20.6 kcal/mol, which indicates that the clusters are efficient Lewis acid catalysts.

For the catalytic tests, the glucose isomerization reaction was carried out in two steps (Figure 9), following the scheme of Saravanamurugan et al.[59,60] In the first step, glucose is isomerized to fructose in the presence of the catalyst. The fructose that is formed immediately reacts with the solvent, ethanol, to form ethyl fructoside. Water is then added in the second step to hydrolyze the fructoside back to fructose. Both steps are carried out at 90 °C. The catalytic performance of the nanocast material was tested against other samples (Table 1), including NU-1000, calcined NU-1000, and control samples of oxozirconium clusters in nontemplated silica supports. As shown in Figure 10, both dehyd-NU-1000 (NU-1000 dehydrated at 300 °C under vacuum to make the oxozirconium clusters Lewis acidic) and the nanocast Zr_6@SiO_2 are active. The rate is slower for Zr_6@SiO_2 which could be due to some of the clusters becoming fully coated with SiO_2 during nanocasting or due to the silica scaffold providing some steric hindrance. Despite this, significant catalytic activity was retained in the nanocast material even after it had been heated to 500 °C. In contrast, bare NU-1000 heated to the same temperature (cal-NU-1000) had very low activity. This shows the importance of maintaining the site isolation in the clusters in order to retain catalytic activity, which was made possible by nanocasting. An XRD pattern of the Zr_6@SiO_2 sample collected after the 72 h catalytic reaction (Figure S12) shows that the broad diffraction features seen for the original sample (Figure 6) are maintained, implying that the clusters remained isolated and did not aggregate during the catalytic reaction. Recycling experiments with Zr_6@SiO_2 show an average loss in glucose conversion of ~13% per cycle over five cycles (Figure S13). The loss in overall activity is more pronounced initially and appears to level off after the third cycle. Interestingly, the fructose yield loss is less pronounced, and as a result, the recycled catalysts become progressively more selective to fructose. It is possible that this is due to reduction of the Brønsted:Lewis acid site ratio with recycling, but further investigations are required to test this hypothesis. Despite these changes, higher catalyst activity is still maintained in recycled Zr_6@SiO_2 as compared to cal-NU-1000. In addition, a higher loading of these site-isolated clusters is also obtained by the nanocasting method than by incorporating oxozirconium clusters in nontemplated silica (Table 1). The nontemplated samples Zr_6@n-t-SiO_2 and Zr_6@n-t-SiO_2(High Zr) exhibit cluster aggregation (Figure S14) despite having a lower Zr loading. Since only micropores are present in both nontemplated samples (Figure S10), the catalytic sites are also less accessible compared to those in the mesoporous nanocast material. This resulted in a significantly lower yield of fructose with Zr_6@n-t-SiO_2 and Zr_6@n-t-SiO_2(High Zr) samples as compared to Zr_6@SiO_2. The ability to retain catalytic activity through site isolation and the templated porosity despite being heated to high temperatures makes nanocasting a useful technique for applying MOF-based catalytic clusters for catalytic processes that may require high temperatures.

■ CONCLUSION

We demonstrated the effectiveness of nanocasting the MOF NU-1000 with silica as a strategy to maintain the catalytic activity of MOF-derived single-site catalytic clusters after high-temperature treatment. Silica coated the larger, 3 nm diameter mesopores, but the precursor did not infiltrate the smaller, 1 nm diameter micropores of NU-1000. Aggregation of oxozirconium clusters to form tetragonal ZrO_2 nanoparticles occurred when NU-1000 was heated to 500 °C in air, but in the nanocast materials no significant cluster agglomeration was observed even after heating to 600 °C in air. The clusters remained accessible to reagents such as pyridine or glucose after these high-temperature treatments. The Lewis acidity of these clusters was demonstrated through the isomerization of

DOI: 10.1021/jacs.5b12688
J. Am. Chem. Soc. 2016, 138, 2739−2748

glucose to fructose, and the mechanism of this reaction was computed with DFT.

The nanocasting method should also be applicable to other large-pore MOF systems that can accommodate precursors like TMOS in the pores. In addition, other precursors could be used for infiltration to produce other secondary scaffold compositions like metal oxides (e.g., titanium dioxide)[35] or carbon by adapting existing nanocasting methods.[32] This affords another handle for optimizing the catalytic properties of the single-site metals or clusters in the nanocast materials. Multiple nanocasting cycles may be used to control the thickness and stability of the secondary scaffold. Nanocasting, combined with the exceptional tunability of MOFs, may pave the way toward a new generation of highly active and stable catalysts for many transformations.

■ ASSOCIATED CONTENT

Supporting Information

The Supporting Information is available free of charge on the ACS Publications website at DOI: 10.1021/jacs.5b12688.

Synthetic methods, characterization of reference samples, alternate synthesis approaches, additional characterization data for SiO_2@NU-1000, mechanism of glucose isomerization on the oxozirconium clusters, catalyst recyling data (PDF)

■ AUTHOR INFORMATION

Corresponding Author

*E-mail: a-stein@umn.edu

Notes

The authors declare no competing financial interest.

■ ACKNOWLEDGMENTS

This research was supported by the U.S. Department of Energy, Office of Basic Energy Sciences, Division of Chemical Sciences under Award DE-SC-0012702, except for the parts listed below. Parts of this work were carried out in the University of Minnesota Characterization Facility, which receives partial support from the NSF through the MRSEC, ERC, MRI, and NNIN programs. The sugar isomerization work was supported as part of the Catalysis Center for Energy Innovation, an Energy Frontier Research Center funded by the U.S. Department of Energy, Office of Science, Basic Energy Sciences under Award DE-SC0001004. Work done at Argonne was performed using the Advanced Photon Source, a U.S. Department of Energy (DOE) Office of Science User Facility operated for the DOE Office of Science by Argonne National Laboratory under Contract No. DE-AC02-06CH11357. A.E.P.P. acknowledges a Beatriu de Pinós fellowship (BP-DGR 2014) from the Ministry of Economy and Knowledge (Catalan Government). We thank Dr. Stephen Rudisill for obtaining SAED patterns.

■ REFERENCES

(1) Thomas, J. M.; Raja, R.; Lewis, D. W. *Angew. Chem., Int. Ed.* **2005**, *44*, 6456.
(2) Liang, S.; Hao, C.; Shi, Y. *ChemCatChem* **2015**, *7*, 2559.
(3) Dal Santo, V.; Guidotti, M.; Psaro, R.; Marchese, L.; Carniato, F.; Bisio, C. *Proc. R. Soc. London, Ser. A* **2012**, *468*, 1904.
(4) Hu, B.; Schweitzer, N. M.; Zhang, G.; Kraft, S. J.; Childers, D. J.; Lanci, M. P.; Miller, J. T.; Hock, A. S. *ACS Catal.* **2015**, *5*, 3494.
(5) Guo, X.; Fang, G.; Li, G.; Ma, H.; Fan, H.; Yu, L.; Ma, C.; Wu, X.; Deng, D.; Wei, M.; Tan, D.; Si, R.; Zhang, S.; Li, J.; Sun, L.; Tang, Z.; Pan, X.; Bao, X. *Science* **2014**, *344*, 616.
(6) Vilé, G.; Albani, D.; Nachtegaal, M.; Chen, Z.; Dontsova, D.; Antonietti, M.; López, N.; Pérez-Ramírez, J. *Angew. Chem., Int. Ed.* **2015**, *54*, 11265.
(7) Yilmaz, B.; Müller, U. *Top. Catal.* **2009**, *52*, 888.
(8) Furukawa, H.; Cordova, K. E.; O'Keeffe, M.; Yaghi, O. M. *Science* **2013**, *341*, 1230444.
(9) Horike, S.; Shimomura, S.; Kitagawa, S. *Nat. Chem.* **2009**, *1*, 695.
(10) Ferey, G. *Chem. Soc. Rev.* **2008**, *37*, 191.
(11) Farha, O. K.; Hupp, J. T. *Acc. Chem. Res.* **2010**, *43*, 1166.
(12) Zhang, T.; Lin, W. *Chem. Soc. Rev.* **2014**, *43*, 5982.
(13) Zhao, M.; Ou, S.; Wu, C.-D. *Acc. Chem. Res.* **2014**, *47*, 1199.
(14) Lee, J.; Farha, O. K.; Roberts, J.; Scheidt, K. A.; Nguyen, S. T.; Hupp, J. T. *Chem. Soc. Rev.* **2009**, *38*, 1450.
(15) Ren, H.-Y.; Yao, R.-X.; Zhang, X.-M. *Inorg. Chem.* **2015**, *54*, 6312.
(16) Mondloch, J. E.; Katz, M. J.; Isley, W. C., III; Ghosh, P.; Liao, P.; Bury, W.; Wagner, G. W.; Hall, M. G.; DeCoste, J. B.; Peterson, G. W.; Snurr, R. Q.; Cramer, C. J.; Hupp, J. T.; Farha, O. K. *Nat. Mater.* **2015**, *14*, 512.
(17) Junghans, U.; Suttkus, C.; Lincke, J.; Lassig, D.; Krautscheid, H.; Glaser, R. *Microporous Mesoporous Mater.* **2015**, *216*, 151.
(18) Deria, P.; Mondloch, J. E.; Karagiaridi, O.; Bury, W.; Hupp, J. T.; Farha, O. K. *Chem. Soc. Rev.* **2014**, *43*, 5896.
(19) Kim, I. S.; Borycz, J.; Platero-Prats, A. E.; Tussupbayev, S.; Wang, T. C.; Farha, O. K.; Hupp, J. T.; Gagliardi, L.; Chapman, K. W.; Cramer, C. J.; Martinson, A. B. F. *Chem. Mater.* **2015**, *27*, 4772.
(20) Mondloch, J. E.; Bury, W.; Fairen-Jimenez, D.; Kwon, S.; DeMarco, E. J.; Weston, M. H.; Sarjeant, A. A.; Nguyen, S. T.; Stair, P. C.; Snurr, R. Q.; Farha, O. K.; Hupp, J. T. *J. Am. Chem. Soc.* **2013**, *135*, 10294.
(21) Gotthardt, M. A.; Schoch, R.; Brunner, T. S.; Bauer, M.; Kleist, W. *ChemPlusChem* **2015**, *80*, 188.
(22) Yang, D.; Odoh, S. O.; Wang, T. C.; Farha, O. K.; Hupp, J. T.; Cramer, C. J.; Gagliardi, L.; Gates, B. C. *J. Am. Chem. Soc.* **2015**, *137*, 7391.
(23) Ranocchiari, M.; Lothschütz, C.; Grolimund, D.; van Bokhoven, J. A. *Proc. R. Soc. London, Ser. A* **2012**, *468*, 1985.
(24) Liu, J.; Lukose, B.; Shekhah, O.; Arslan, H. K.; Weidler, P.; Gliemann, H.; Bräse, S.; Grosjean, S.; Godt, A.; Feng, X.; Müllen, K.; Magdau, I.-B.; Heine, T.; Wöll, C. *Sci. Rep.* **2012**, *2*, 921.
(25) Deng, H.; Grunder, S.; Cordova, K. E.; Valente, C.; Furukawa, H.; Hmadeh, M.; Gándara, F.; Whalley, A. C.; Liu, Z.; Asahina, S.; Kazumori, H.; O'Keeffe, M.; Terasaki, O.; Stoddart, J. F.; Yaghi, O. M. *Science* **2012**, *336*, 1018.
(26) Ma, S.; Wang, X.-S.; Yuan, D.; Zhou, H.-C. *Angew. Chem., Int. Ed.* **2008**, *47*, 4130.
(27) Cavka, J. H.; Jakobsen, S.; Olsbye, U.; Guillou, N.; Lamberti, C.; Bordiga, S.; Lillerud, K. P. *J. Am. Chem. Soc.* **2008**, *130*, 13850.
(28) Kang, I. J.; Khan, N. A.; Haque, E.; Jhung, S. H. *Chem. - Eur. J.* **2011**, *17*, 6437.
(29) Zhang, L.; Hu, Y. H. *J. Phys. Chem. C* **2010**, *114*, 2566.
(30) Sattler, J. J. H. B.; Ruiz-Martinez, J.; Santillan-Jimenez, E.; Weckhuysen, B. M. *Chem. Rev.* **2014**, *114*, 10613.
(31) LeValley, T. L.; Richard, A. R.; Fan, M. *Int. J. Hydrogen Energy* **2014**, *39*, 16983.
(32) Lu, A. H.; Schüth, F. *Adv. Mater.* **2006**, *18*, 1793.
(33) Lu, C.; Ben, T.; Xu, S.; Qiu, S. *Angew. Chem., Int. Ed.* **2014**, *53*, 6454.
(34) Sun, J.-K.; Xu, Q. *Energy Environ. Sci.* **2014**, *7*, 2071.
(35) Hall, A. S.; Kondo, A.; Maeda, K.; Mallouk, T. E. *J. Am. Chem. Soc.* **2013**, *135*, 16276.
(36) Leong, K.; Foster, M. E.; Wong, B. M.; Spoerke, E. D.; Van Gough, D.; Deaton, J. C.; Allendorf, M. D. *J. Mater. Chem. A* **2014**, *2*, 3389.
(37) Sabo, M.; Henschel, A.; Frode, H.; Klemm, E.; Kaskel, S. *J. Mater. Chem.* **2007**, *17*, 3827.

DOI: 10.1021/jacs.5b12688
J. Am. Chem. Soc. 2016, 138, 2739−2748

(38) Talin, A. A.; Centrone, A.; Ford, A. C.; Foster, M. E.; Stavila, V.; Haney, P.; Kinney, R. A.; Szalai, V.; El Gabaly, F.; Yoon, H. P.; Léonard, F.; Allendorf, M. D. *Science* **2014**, *343*, 66.
(39) Planas, N.; Mondloch, J. E.; Tussupbayev, S.; Borycz, J.; Gagliardi, L.; Hupp, J. T.; Farha, O. K.; Cramer, C. J. *J. Phys. Chem. Lett.* **2014**, *5*, 3716.
(40) Zhao, Y.; Truhlar, D. G. *J. Chem. Phys.* **2006**, *125*, 194101.
(41) Frisch, M. J.; Trucks, G. W.; Schlegel, H. B.; Scuseria, G. E.; Robb, M. A.; Cheeseman, J. R.; Scalmani, G.; Barone, V.; Mennucci, B.; Petersson, G. A.; Nakatsuji, H.; Caricato, M.; Li, X.; Hratchian, H. P.; Izmaylov, A. F.; Bloino, J.; Zheng, G.; Sonnenberg, J. L.; Hada, M.; Ehara, M.; Toyota, K.; Fukuda, R.; Hasegawa, J.; Ishida, M.; Nakajima, T.; Honda, Y.; Kitao, O.; Nakai, H.; Vreven, T.; Montgomery, J. A., Jr.; Peralta, J. E.; Ogliaro, F.; Bearpark, M.; Heyd, J. J.; Brothers, E.; Kudin, K. N.; Staroverov, V. N.; Kobayashi, R.; Normand, J.; Raghavachari, K.; Rendell, A.; Burant, J. C.; Iyengar, S. S.; Tomasi, J.; Cossi, M.; Rega, N.; Millam, J. M.; Klene, M.; Knox, J. E.; Cross, J. B.; Bakken, V.; Adamo, C.; Jaramillo, J.; Gomperts, R.; Stratmann, R. E.; Yazyev, O.; Austin, A. J.; Cammi, R.; Pomelli, C.; Ochterski, J. W.; Martin, R. L.; Morokuma, K.; Zakrzewski, V. G.; Voth, G. A.; Salvador, P.; Dannenberg, J. J.; Dapprich, S.; Daniels, A. D.; Farkas, Ö.; Foresman, J. B.; Ortiz, J. V.; Cioslowski, J.; Fox, D. J. *Gaussian 09*, revision D.01; Gaussian Inc.: Wallingord, CT, 2009.
(42) Zhao, Y.; Peverari, R.; Yang, K.; Truhlar, D. G. *MN-GFM*, version 6.4; University of Minnesota: Minneapolis, MN, 2012.
(43) Nicklass, A.; Dolg, M.; Stoll, H.; Preuss, H. *J. Chem. Phys.* **1995**, *102*, 8942.
(44) Weigend, F.; Ahlrichs, R. *Phys. Chem. Chem. Phys.* **2005**, *7*, 3297.
(45) Macrae, C. F.; Edgington, P. R.; McCabe, P.; Pidcock, E.; Shields, G. P.; Taylor, R.; Towler, M.; van de Streek, J. *J. Appl. Crystallogr.* **2006**, *39*, 453.
(46) Hammersley, A. P.; Svensson, S. O.; Hanfland, M.; Fitch, A. N.; Hausermann, D. *High Pressure Res.* **1996**, *14*, 235.
(47) Jennings, G. *QXRD*, version 0.11.10.; Argonne National Laboratory: Lemont, IL, 2015.
(48) Yakovenko, A. A.; Reibenspies, J. H.; Bhuvanesh, N.; Zhou, H.-C. *J. Appl. Crystallogr.* **2013**, *46*, 346.
(49) Yakovenko, A. A.; Wei, Z.; Wriedt, M.; Li, J.-R.; Halder, G. J.; Zhou, H.-C. *Cryst. Growth Des.* **2014**, *14*, 5397.
(50) Le Bail, A. *J. Non-Cryst. Solids* **1995**, *183*, 39.
(51) Petříček, V.; Dušek, M.; Palatinus, L. *Z. Kristallogr. - Cryst. Mater.* **2014**, *229*, 345.
(52) Wojdyr, M. *J. Appl. Crystallogr.* **2010**, *43*, 1126.
(53) McCusker, L. B.; Baerlocher, C. *Chem. Commun.* **2009**, 1439.
(54) Qiu, X.; Thompson, J. W.; Billinge, S. J. L. *J. Appl. Crystallogr.* **2004**, *37*, 678.
(55) Zaki, M. I.; Hasan, M. A.; Al-Sagheer, F. A.; Pasupulety, L. *Colloids Surf., A* **2001**, *190*, 261.
(56) Kline, C. H.; Turkevich, J. *J. Chem. Phys.* **1944**, *12*, 300.
(57) Bagshaw, S. A.; Cooney, R. P. *Chem. Mater.* **1993**, *5*, 1101.
(58) Rosenberg, D. J.; Anderson, J. A. *Catal. Lett.* **2002**, *83*, 59.
(59) Saravanamurugan, S.; Paniagua, M.; Melero, J. A.; Riisager, A. *J. Am. Chem. Soc.* **2013**, *135*, 5246.
(60) Ren, L.; Guo, Q.; Kumar, P.; Orazov, M.; Xu, D.; Alhassan, S. M.; Mkhoyan, K. A.; Davis, M. E.; Tsapatsis, M. *Angew. Chem., Int. Ed.* **2015**, *54*, 10848.

DOI: 10.1021/jacs.5b12688
J. Am. Chem. Soc. 2016, 138, 2739−2748